

Stress Calculation and Fatigue Life Evaluation on Cup-Type Flexspline under Bending and Torsion in Harmonic Drive

Ligang Cai*, Qiushi Hu**, Zhifeng Liu*, Congbin Yang***
and Tao Zhang**

Keywords : Harmonic drive, Flexspline, Multi-tooth meshing, Fatigue life evaluation.

ABSTRACT

This paper describes a composite method of calculating multi-tooth root stress and evaluating fatigue life of flexspline (FS) in harmonic drive (HD). In order to accurately describe the stress state of the flexible gear root, a mathematical method combined with simulation method is applied. FS is divided into two parts, the cup part and the teeth part, according to the type of stress. On the cup part, the stress is caused by the support of the wave generator (WG). The bending stress is analyzed using differential equations and appropriately set boundary conditions. The theoretical analysis of meshing teeth in a harmonic drive is brought into the finite element model of FS that is deformed by the outer contour of the wave generator. The simulation is conducted under the action of torque and the meshing generated stress is obtained. Finally, the stress spectrum of the tooth root is acquired according to the flexural and torsion stress, while the maximum radial, the circumferential and shear stress are obtained. After applying the fourth strength theory to calculate the Von-Mises stress, the safety factors of several materials are compared according to the S-N curve and fatigue limit formula.

INTRODUCTION

Paper Received January, 2019. Revised June, 2019, Accepted July, 2019, Author for Correspondence: Zhifeng Liu.

* Professor, Institute of Advanced Manufacturing and Intelligent Technology, Beijing University of Technology, Beijing 100124, China.

** PH. D student, Institute of Advanced Manufacturing and Intelligent Technology, Beijing University of Technology, Beijing 100124, China.

*** Lecturer, Institute of Advanced Manufacturing and Intelligent Technology, Beijing University of Technology, Beijing 100124, China.

Due to the increasing demand for high ratio, improved transmission accuracy and bearing capacity of speed reducers in the modern industry, the harmonic reducer is widely used in robotics, space technology, energy, bionic and marine engineering (Musser,1959,1996). Since it was first introduced, the harmonic speed reducer has attracted the attention of scholars all over the world, for its distinctive driving characteristics. Although extensive research work in the design, dynamics and experimental aspects has been carried out (Vassileva et al., 2011; Liu 2006), offering a series of useful results, there are still many issues to be explored (Zou et al., 2013; Zu et al., 2016).

The structure of the cup-type harmonic speed reducer is relatively simple, as shown in Figure 1. It mainly consists of five parts: (a) Wave generator (WG): a mandrel with an elliptic outer profile, rotates a flexspline (FS) along an elliptical path, thereby realizing a relative rotation. (b) Flexible bearing (FB): arranged on the outer side of the wave generator to reduce friction, improving transmission efficiency. (c) Flexspline (FS): a cup shaped short tube with outer teeth, being the core component, determining the performance of the harmonic drive. (d) Circular spline (CS): assigned to realize the relative rotation of FS in general. (e) Cross roller bearing (CRB): the output of the harmonic drive.

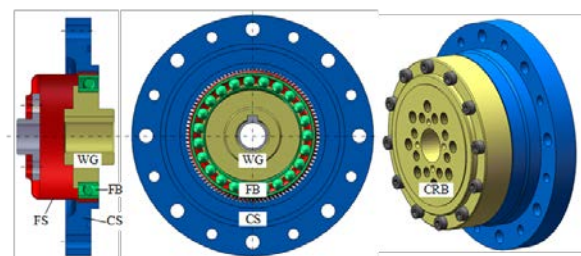


Fig. 1. Typical structure of a cup-type harmonic drive

In order to study the characteristics of the HD, researchers have tried to systematically analyze the harmonic reducers in various ways. Tuttle (1992) studied the stiffness, friction and motion error of the

harmonic drive, and described their nonlinear behaviors. Jeong (1995) improved the torsional rigidity of FS by using composite material in view of the characteristics. The test results showed that the composite material had remarkable effect on improving the radial flexibility. Gandhi (2001) studied the characteristics of harmonic drive and proposed a nonlinear control algorithm to improve the transmitting performance. Preissner (2012) treated the harmonic drive as a black box to discuss four key aspects: nonlinear viscous friction, nonlinear stiffness, hysteresis, kinematic error. He combined nonlinear friction and a kinematic error model to obtain an accurate description. Ma (2016) used computer vision technology to identify the meshing process of FS with circular spline and its corresponding frictional behavior in harmonic drive. Chao (2015) established an accelerated experimental model and a genetic algorithm, where the fatigue failure process is described by using the Manson fatigue failure rule. Gravagno (2016) observed the relationship between the outer ring curve of wave generator and FS, deriving an analytic expression of the relative rotation.

Zhang (2014) presented a new model of torsional compliance and hysteretic characteristics of harmonic drive system based on the behavior of FS. The soundness of the model was verified by numerical simulations and experiments. Chen (2014) studied the influence of double circular arc profile on the gear engagement of harmonic drive. His results showed that this method can effectively improve the transmission performance. Tjahjowidodo (2013) offered a new model for torsional compliance, using the Maxwell-slips model, and verified the its validity for different torque values. Han (2016) modeled the nonlinear friction behavior of the harmonic drive by the DGCMG (double-gimbal control momentum gyro) method, where the feedforward compensation controller based on the improved model was designed to compensate the friction force. Gao (2004) presented a new method for measuring the errors of FS, by using double laser probes, achieving accuracy up to $\pm 2\mu\text{m}$. Shi (2017) proposed a joint torque calculation model based on a harmonic drive model, compared it with the other two existing methods, and proved its validity. Routh (2014) focused on lubrication, producing the analytical expressions for lubricant film separation and other lubrication conditions under general boundary conditions.

Ostapski (2007, 2011) established a model by using the analytical description of the harmonic drive, producing a more adequate three-dimensional model, using the finite element method (FEM). Kikuchi (2003) carried out the stress analysis of FS based on the beam element and verified, by simulation, the feasibility of the theoretical calculations. Han (1999) studied the stress and vibration of composite and alloy steel material, where the damping, natural

frequency and stiffness of the composite versus the alloy steel were compared. Kayabasi (2007) set the stress and fatigue safety factor as the goal, optimizing the parameters of the flexible gear teeth based on an algorithm, and obtained higher safety factor, based on Ansys. Folega (2013) carried out the stress analysis using the boundary element method and studied the effect of design parameters on the stress of the root, producing an effective method to reduce the stress. Xiang (2014) calculated the geometrical characteristics and mechanical properties of FS based on the thin shell model. The stress equations of the inner and outer surfaces of FS are obtained by introducing the temperature factor. Finally, the FEM is used to verify the stress equation. Sahoo (2015) studied the equivalent stress of different positions of FS cup based on the FEM and verified it experimentally.

To summarize, theoretical calculation and simulation are two main methods for analyzing the tooth root stress. Due to the complex structure of FS, it is difficult to calculate using only theoretical approach. The solution of tooth root stress is mostly realized by FEM that leads to an inaccurate result. We need to find an effective and accurate method that distinguishes between different stress forms of FS and then calculates them separately. On the cup body part, the bending stress is analyzed using the thin-walled cylinder theory; on the teeth part, FEM is used to calculate the meshing stress. Von-Mises stress is obtained combining these two kinds of stress. Finally, fatigue life evaluation can be carried out based on Geber and Goodman fatigue limit formulas.

In this paper, a quasi-steady state model of fluid bulk within the tank is established and integrated with the multiple steering yaw/roll model to investigate the directional response at constant forward speed with steady steer input. The influences of the additional steering wheel on the yaw/roll motions, filling variation and liquid load shift on the steering response of the tank vehicle are studied and compared to that of traditional vehicle with single steering to demonstrate that the multiple steering increases the maneuverability and decreases the destabilizing effects of liquid load shift.

MOEDLING OF BENDING AND MESHING STRESS

The calculation of alternating stress is the basis of the performance of FS, however, the research on this aspect is less than exhausting. The solution of tooth root stress is mostly realized by FEM, but the results cannot accurately enough describe the complex multi-tooth meshing stress state. Fig.2 presents the structure flow of this article. First, a composite method of stress extraction is carried out by studying two different types of stress: the bending

stress and the meshing stress. The stress spectrum is obtained by coupling the two previous results, and finally, fatigue life evaluation is carried out.

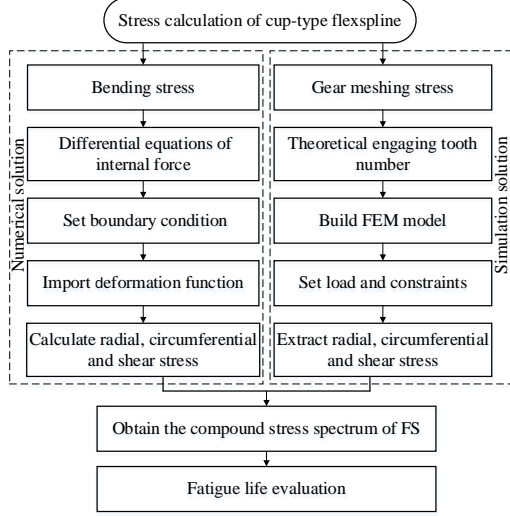


Fig. 2. The flow chat of stress extraction and fatigue life evaluation of FS

Theoretical solution model of bending stress

The deformation of FS, as shown in Fig. 3, produces elastic deformation under the support of the wave generator. The force in the meshing region (CD and EF), especially on the long axis (AA') reaches its maximum value, while on the short axis displays zero.

Due to the low thickness of FS, and to the diameter-thickness ratio being much higher than 20, FS model is simplified as a thin shell, ignoring the influence of the tooth.

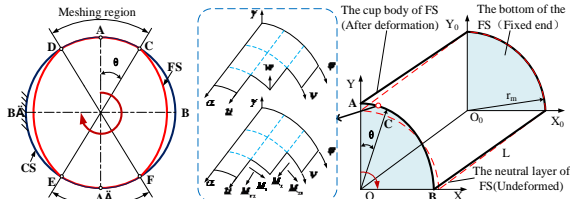


Fig. 3. Displacement and internal force distribution of FS

The geometric equations (Xu, 2016) of FS shells can be written as:

$$\begin{cases} \varepsilon_\alpha = \frac{\partial u}{\partial \alpha}, \varepsilon_\varphi = \frac{\partial v}{\partial \varphi} + \frac{w}{r}, \varepsilon_{\alpha\varphi} = \frac{\partial u}{\partial \alpha} + \frac{\partial v}{\partial \varphi} \\ \chi_\alpha = -\frac{\partial^2 w}{\partial \alpha^2}, \chi_\varphi = -\frac{\partial^2 w}{\partial \varphi^2}, \chi_{\alpha\varphi} = -\frac{\partial^2 w}{\partial \alpha \partial \varphi} \end{cases} \quad (1)$$

Where, ε_α is strain in the direction of α ; ε_φ is strain in the direction of φ , $\varepsilon_{\alpha\varphi}$ is shear strain on the middle surface of FS; u is displacement in the α direction; v is displacement in the φ direction; w is displacement in the γ direction; χ_α , χ_φ , $\chi_{\alpha\varphi}$ are twist

rate of each point respectively.

The physical equations (Ren, 2012) of FS shells can be drawn as:

$$\begin{cases} N_1 = \frac{Eh}{1-\mu^2}(\varepsilon_\alpha + \mu\varepsilon_\varphi) \\ N_2 = \frac{Eh}{1-\mu^2}(\varepsilon_\varphi + \mu\varepsilon_\alpha) \\ S_{12} = S_{21} = \frac{Eh}{2(1+\mu)}\varepsilon_{\alpha\varphi} \\ M_1 = \frac{Eh^3}{12(1-\mu^2)}(\chi_\alpha + \mu\chi_\varphi) \\ M_2 = \frac{Eh^3}{12(1-\mu^2)}(\chi_\varphi + \mu\chi_\alpha) \\ M_{12} = \frac{Eh^3}{12(1+\mu)}\chi_{\alpha\varphi} \end{cases} \quad (2)$$

Where, E is modulus of elasticity; μ is Poisson's ratio; N_1 , N_2 are tension and pressure force; S_{12} is normal force; M_1 , M_2 are bending moments; M_{12} is torque.

According to the linear assumption of the center line of FS, the boundary condition is:

$$\begin{cases} (u, v, w, \partial w / \partial \alpha)_{\alpha=0} = 0 \\ (N_1, S, M_1, Q_1)_{\alpha=l} = 0 \end{cases} \quad (3)$$

An orthogonal coordinate system is set up on the curved surface of FS, in which α and φ means the principal curvature lines on the middle surface, and γ is the normal axis perpendicular to the middle surface. The range of γ is $[-h/2, h/2]$.

The stresses of FS can be expressed as:

$$\begin{cases} \sigma_1 = \frac{E}{1-\mu^2} \left[\frac{\partial u}{\partial \alpha} + \mu \left(\frac{\partial v}{\partial \varphi} + \frac{w}{r} \right) \right] \\ - \frac{12D\gamma}{h^3} \left[\frac{\partial^2 w}{\partial \alpha^2} + \mu \frac{\partial^2 w}{\partial \varphi^2} \right] \\ \sigma_2 = \frac{E}{1-\mu^2} \left(\frac{\partial v}{\partial \varphi} + \frac{w}{r} + \mu \frac{\partial u}{\partial \alpha} \right) \\ - \frac{12D\gamma}{h^3} \left[\frac{\partial^2 w}{\partial \varphi^2} + \mu \frac{\partial^2 w}{\partial \alpha^2} \right] \\ \tau_{12} = \tau_{21} = \frac{E}{2(1+\mu)} \left(\frac{\partial u}{\partial \alpha} + \frac{\partial v}{\partial \varphi} \right) \\ - \frac{12D(1-\mu)\gamma}{h^3} \frac{\partial^2 w}{\partial \alpha \partial \varphi} \end{cases} \quad (4)$$

Where D is column stiffness, $D = Eh^3/12(1-\mu^2)$.

It is known that σ_1 , σ_2 and τ_{12} are three dimensional functions on α , φ , γ . When given certain

values, the stress distribution of FS can be obtained.

Meshing stress calculation of FS by FEM

Since the complexity and unpredictability of gear engagement in work, it's effective and practical to acquire the meshing stress of FS by using FEM. Fig. 5 gives a detailed description of the FEM model applied to meshing stress calculation. The meshing process between FS and CS is divided into three stages: disengaged, half engagement and full engagement. The changes of these stages are caused by the tooth Mesh in and out. As the wave number of WG is two, the teeth at the two regions are under the same meshing conditions, so it is enough to discuss one meshing region. Considering the uncertainty of meshing teeth number, the number of engaging teeth is theoretically calculated in the next section.

Calculation of theoretical engaging teeth number

The arc length of a harmonic gear drive refers to the length of the arc along which the pair of teeth begin to mesh until the end of the engagement. We think that the coordinates of the top of FS gear should be the same as those of CS gear in {XOY} coordinate system at the moment of approaching action or receding action. From Fig. 4, the polar radius of the two states exhibits equally in the coordinate system.

$$\sqrt{x_a^2 + y_a^2} = \sqrt{x_b^2 + y_b^2} = r_a = r_b \tag{5}$$

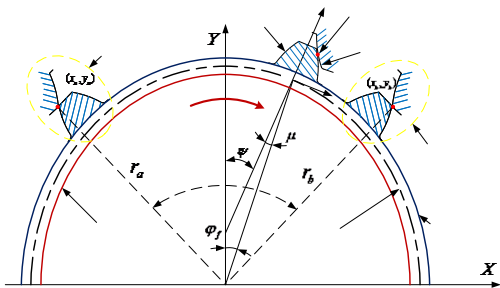


Fig. 4. Coordinate transformation in CS coordinate system

The assumption that the CS is fixed, and FS tooth profile curve is expressed in coordinates {X1O1Y1}, forces the transformation into the fixed coordinate system {XOY}. The angle between the two coordinate systems is: $\psi = \varphi_f + \mu$. Within the rotating wave generator, the addendum coordinates of FS can be obtained at any position of the top. Given that the wave generator turns around in an angle φ_H , the rotation angle φ_f of FS can be given as:

$$\varphi_f = \frac{U \varphi_H}{z} + \frac{v}{r_m} \tag{6}$$

Where U is wave number of Wave generator; z is the number of FS teeth; φ_H is rotation angle of the wave generator; v is tangential displacement of FS; r_m

is radius of center line of FS before deformation.

When FS is deformed, under the condition that the center line is not elongated, the symmetry axis of FS teeth rotates at an angle μ_f from the radius, in addition to radial and tangential displacements. The relationship between μ_f and polar radius ρ of FS can be displayed in Eq. (7).

$$\mu_f = \arctan \frac{d\rho/d\varphi_f}{\rho} \tag{7}$$

Therefore, according to the transformation relation from coordinates system {X1O1Y1} to coordinates system {XOY}, the coordinates of FS tooth curve are demonstrated by Eq. (8).

$$\begin{Bmatrix} X \\ Y \\ 1 \end{Bmatrix} = \begin{pmatrix} \cos \psi & \sin \psi & \rho \sin \varphi_f \\ -\sin \psi & \cos \psi & \rho \cos \varphi_f \\ 0 & 0 & 1 \end{pmatrix} \begin{Bmatrix} x_1 \\ y_1 \\ 1 \end{Bmatrix} \tag{8}$$

On the basis of Eq. (5) ~ Eq. (8), Eq. (9) for solving the coordinates at the moment of approaching action or receding action can be obtained:

$$\begin{aligned} x_1^2 + y_1^2 + \rho^2 - 2x_1y_1 \sin \mu_f \\ - 2\rho(x_1 \sin \mu_f - y_1 \cos \mu) - r_a^2 = 0 \end{aligned} \tag{9}$$

Where r_a is addendum radius of CS, $\{x_1, y_1\}$ are the coordinates of the top of FS gear tooth in {X1O1Y1}. Since φ_f can be calculated by the upper formula, the logarithmic teeth number N can be next obtained to be used in the simulation analysis.

Procedures of a developmental FEM method

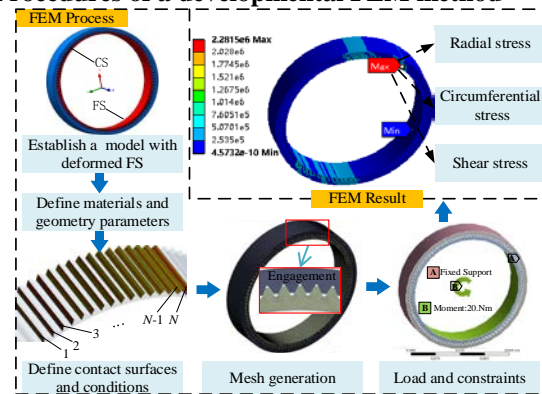


Fig. 5. The process of the developmental FEM for extracting meshing stress

In this paper, a developmental FEM method is innovatively applied to extracting meshing stress. The primary advantage of this method lies in the simulation of deformed FS model, which avoids the influence of bending stress on meshing stress. Fig. 5 shows the teeth of FS in the meshing tooth area. In

order to characterize the different meshing position in relation to the stress conditions, these teeth are numbered starting from 1 to N .

Step 1: Establish a model with deformable FS according to FS deformation function. The model consists of the gear part alone and does not contain the cup part. Assemble it with the CS model.

Step 2: Define materials and geometry parameters. Determine material parameters such as density, modulus of elasticity and Poisson's ratio of FS and CS. Establishing a cylindrical coordinate system with the geometric center of FS as the origin.

Step 3: Define the contact surface of FS and CS. The teeth surface of FS is the contact surface, while the teeth surface of CS is the target surface. In order to set the real contact surface conditions, according to Eq.16, the quantity of contact surfaces is N , each interval has N FS and CS teeth. In order to characterize the different meshing position in relation to the stress conditions, these teeth are numbered starting from 1 to N .

Step 4: Define contact conditions of FS and CS. The type of contact conditions is frictional, friction coefficient is 0.15, the formulation is 'Augment Lagrange', normal stiffness factor is 0.02 and the interface set 'adjust to touch'.

Step 5: Mesh generation. Mesh generation of FS and CS is accomplished by sweep, and the mesh of teeth surface need to be refined.

Step 6: Set load and constraints. Define CS as fixed support. Applying torque to FS, torque values range from 0 to the limit torque, increasing at a step of 10 Nm.

Step 7: Extraction of meshing stress. Derive the maximum radial, circumferential and shear stress of the teeth root in the cylindrical coordinates system established in step 2. In this step, in order to extract the stress in the whole meshing process, it is necessary to extract the root stress from numbered 1 to N , which was set in step 3.

Step 8: End of the analysis.

Validation of FEM model

Hertz contact theory is well known for analyzing the local strain and stress distribution of two objects under compressive contact. The theory is based on three assumptions: (1) A small deformation occurs in the contact area; (2) The contact surface is elliptical; (3) the objects in contact can be regarded as an elastic half space, and the contact surface refers only to the distributed vertical pressure. The tooth surface of the involute gear of the harmonic reducer is a special curved surface with complex shape, where the width of the contact area is less than the curvature radius of the tooth surface within the contact area.

$$\sigma_H = \sqrt{\frac{1}{\pi} \cdot \frac{F_t \cos \beta \cos \alpha'_i}{b \cos^2 \alpha_i \left(\frac{1-\mu_1^2}{E_1} + \frac{1-\mu_2^2}{E_2} \right)} \cdot \frac{u_i+1}{u_i} \cdot \frac{2 \cos \beta}{d_1 \sin \alpha_i}} \quad (10)$$

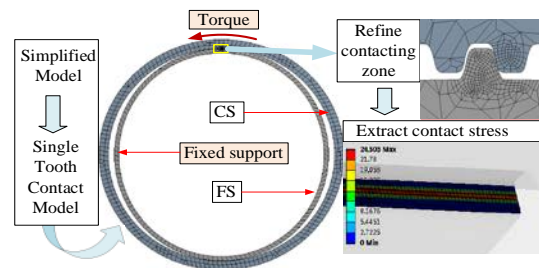
The maximum contact stress of involute gear σ_H (Fu, 2007) can be presented by Eq. (10).

Where, F_t is tangential force, α_i is pitch circle pressure angle, α'_i is meshing angle, T is load torque, K is the load factor, $F_t = 2KT/d_1(\cos \alpha_i/\cos \alpha'_i)$, β is helix angle, b is Tooth width, μ_1 and μ_2 is Poisson's ratio, E_1 and E_2 is modulus of elasticity, u_i is transmission ratio, d_1 is indexing circle diameter.

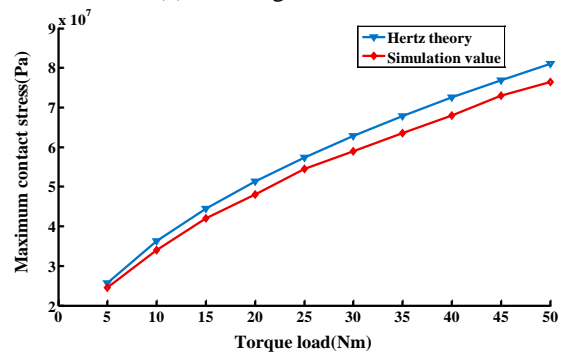
The meshing simulation modeling process of WG-FS involute tooth profile of harmonic drive can be summarized as follows. (1) The involute tooth profile of WG is deduced from the equation of the involute tooth profile of FS, according to the meshing principle and then the three-dimensional model of the WG-FS is established. (2) In the setting of the simulation model, the material properties are introduced in Tab. 1. The meshing part is line contact, and the mesh of the contact tooth pair is refined; the mesh of the unrelated part is set thicker, and finally fixed by the inner wall of FS; the CS applies torque to simulate the contact condition of the tooth pair. (3) In the simulation process, the torque exerted by CS ranges from 5 Nm, increasing at a 5 Nm step and reaching the upper limit of torque at 50 Nm.

Tab. 1. Material properties of FS and CS

Materials	Modulus of elasticity ($\times 10^5$ MPa)	Poisson's ratio	Density (g/cm ³)
FS	2.09	0.295	7.87
CS	2.11	0.277	7.87



(a) Building FEM model



(b) Results comparison

Fig.6. The validation process of FEM model

Fig.6 (b) reveals the maximum contact stress under FEM simulation and Hertz theory within a certain range of torque load. The maximum deviation between simulation results and theoretical results is less than 10%, verifying the reliability of the simulation model. Therefore, it can be said that the proposed simulation model is suitable for the description of the involute CS and FS in harmonic drive.

EXAMPLE ANALYSIS OF HARMONIC DRIVE CSG20-50

Let us take the case of CSG20-50 as an example for the implementation of the proposed process. Firstly, the bending stress and torsional stress of the harmonic drive are solved separately, and then coupled together to calculate the compound stress of multi-tooth.

Bending stress solution

The relating structural parameters of CSG20-50 are listed in Tab.2.

Tab. 2. Structural parameters of CSG20-50

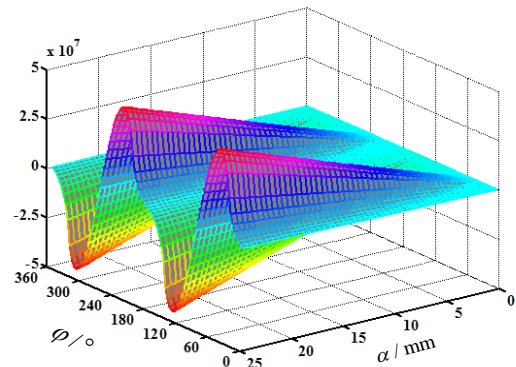
Parameters	values
Transmission ratio	50
Tooth number of FS	100
Length of FS	25
Thickness of FS	0.3
Pitch radius of FS (r_a)	25.4
Deformation coefficient (ω_0)	0.396

There are many kind of materials for making FS. In this paper, four typical FS materials are selected: 12Cr2Ni4, 20CrMnSi, 30CrMoA and 40CrNiMoA. Their density, modulus of elasticity and Poisson's ratio are shown in Tab. 3.

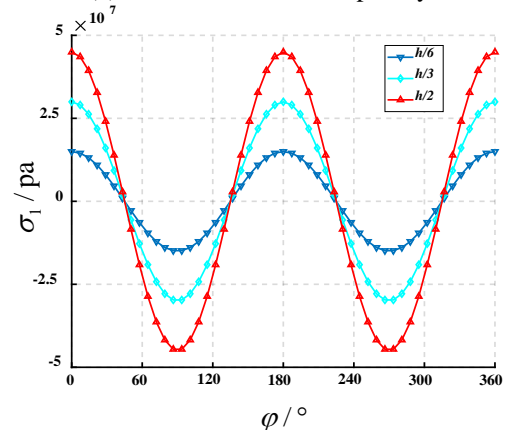
Tab. 3. Physical properties of four typical FS materials

Materials	Density (g/cm ³)	Modulus of elasticity (×10 ⁵ MPa)	Poisson's ratio
12Cr2Ni4	7.84	2.07	0.298
20CrMnSi	7.80	2.10	0.276
30CrMoA	7.85	2.11	0.279
40CrNiMoA	7.87	2.09	0.295

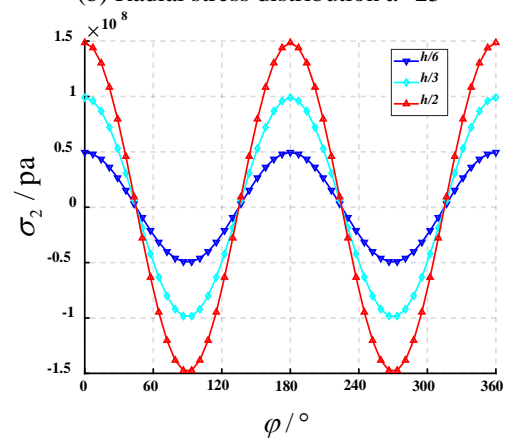
The FS deformation function $\omega = \omega_0 \alpha \cos 2\varphi / l$. Where ω_0 is deformation coefficient, a is the distance to the bottom of FS, l is the length of FS. The bending stress can be obtained when bringing the parameters of Tab. 2 and Tab. 3 into Eq. (4). Taking the material 40CrNiMoA as an example, after a series of calculation by computer, the distribution of the bending stress of this material can be presented in Fig.7.



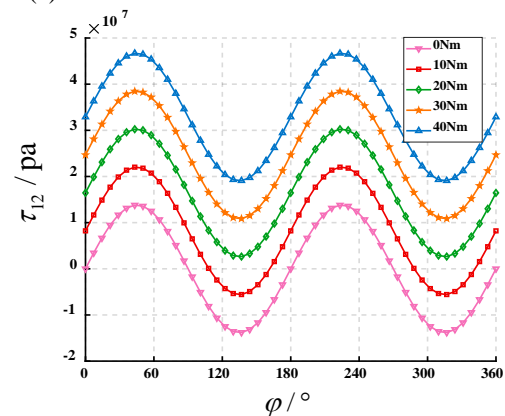
(a) Radial stress of FS cup body



(b) Radial stress distribution $a=25$



(c) Circumferential stress distribution $a=25$



(d) Shear stress distribution under different torque
Fig. 7. Distribution of the bending stress

From Fig. 7, it can be seen that there is a strong periodicity in the distribution of bending stress. In terms of amplitude, the circumferential stress amplitude is the largest and the shear stress is the smallest. Radial stress and circumferential stress have the same periodicity and variation rule, which means the maximum value appears at 0 and 180 degrees while the minimum value is exist at 90 and 270 degrees. The stress value increases with the increase of thickness. In addition, the extreme and average values of the shear stress increase with the adding of the torque, but the amplitude stays the same.

Meshing stress analysis

The meshing stress of tooth surface is much more complicated. After numbering each meshing pair, the root stress of FS is derived according to the simulation process in last chapter. By calculating with the geometric parameters of CSG20-50, the meshing teeth number N is 16 and the calculated meshing stress is displayed in Fig.8.

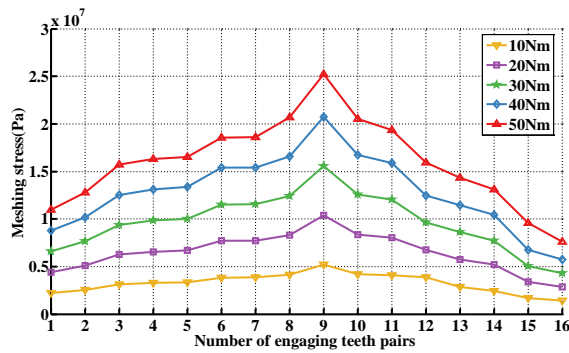


Fig. 8. The meshing stress of different engaging teeth

In the zone of engaging-in, meshing stress value increases as the meshing depth increases, while the maximum stress point is located at the 9th teeth pair. The pairs 10th-16th consist the zone of engaging-out, where meshing stress value decreases as the rotation angle increases. Overall, the average stress in the zone of engaging-in is higher than that in the zone of engaging-out as a result of the impact of engaging.

Compound stress of FS

The stress of FS is composed of bending and meshing stress. The bending stress can be obtained by theoretical calculation approach, while the torsion stress can be acquired by FEM. The coupling effect between bending and meshing stress is not taken into account. In the cases of radial and circumferential stress, the tensile component of stress is positive (+) and the compressive component is negative (-). In the case of shear stress, clockwise is considered as positive (+) and counterclockwise is the negative (-). The root of the teeth is the weakest point in the whole FS, as far as fatigue life is concerned. In order to acquire the compound stress, the calculated radial, circumferential and shear stress are added with those

stress by simulating respectively in last section. Tab. 4 demonstrates the compound stress of four typical FS materials.

Tab. 4. The values of compound stress derived of four typical FS materials

Materials	Radial		Circumferential		Shear	
	Min	Max	Min	Max	Min	Max
12Cr2Ni4	-147.8	158.1	-40.6	58.5	14.5	59.5
20CrMnSi	-147.5	157.9	-40.7	61.1	14.0	60.1
30CrMoA	-148.5	159.2	-41.4	62.2	13.9	60.1
40CrNiM oA	-148.6	158.9	-43.8	63.4	14.1	59.6

Fatigue life extraction

On a single tooth of FS, the stress follows along a pulse cycle. Whether the tooth root material can produce fatigue failure can be judged by the Haigh Diagram (Fatigue limit diagram). The fatigue limit diagram is different fatigue limit stress of different stress ratios was plotted on one diagram in the specified destruction cycle life.

At present, the fatigue life calculation is mainly based on Gerber and Goodman fatigue theories, as illustrated in Tab. 5.

Tab. 5. Fatigue formulas and safety factor

Fatigue theories	Fatigue formulas	Safety factor (S)
Gerber	$\sigma_a = \sigma_{-1} [1 - (\frac{\sigma_m}{\sigma_b})^2]$	$\frac{S\sigma_a}{\sigma_{-1}} + (\frac{S\sigma_m}{\sigma_b})^2 = 1$
Goodman	$\sigma_a = \sigma_{-1} (1 - \frac{\sigma_m}{\sigma_b})$	$\frac{\sigma_a}{\sigma_{-1}} + \frac{\sigma_m}{\sigma_b} = \frac{1}{S}$

As seen from Tab.5, the fatigue life safety factor of FS is represented by S ; σ_{-1} is ultimate fatigue stress under symmetrical cyclic loading, as derived by the $S-N$ curve (Stress-life curve) of the material; σ_b is strength limit of materials; σ_m is the mean stress and σ_a is stress amplitude, all derived from Eq. (11):

$$\sigma_m = \frac{(\sigma_{\max} + \sigma_{\min})}{2} \quad \sigma_a = \frac{(\sigma_{\max} - \sigma_{\min})}{2} \quad (11)$$

The $S-N$ curve of fatigue life of materials is continuously declining, which can be described by Basquin equation (Starke et al., 2010):

$$\sigma_a = \sigma'_f (2N_f)^{b'} \quad (12)$$

Where, σ'_f is fatigue strength factor, N_f is number of fatigue failure cycles, b' is Basquin index. The high-cycle $S-N$ curves of 12Cr2Ni4, 20CrMnSi, 30CrMoA and 40CrNiMoA are presented in Fig. 9.

The cup-type FS is a thin walled cylindrical specimen under regular plastic deformation. Additionally, the composite stress fatigue strength

criterion is suitable for the fatigue strength calculation of bending and torsion of composite circular shafts. Therefore, the deviator strain energy theory (the 4th strength theory) can be used to predict the fatigue life of FS.

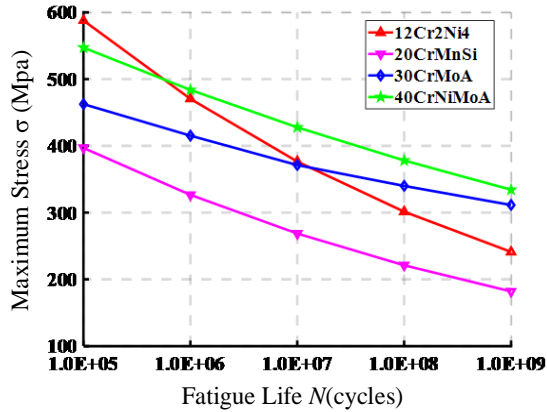


Fig. 9. High-cycle S-N curves of four typical FS materials

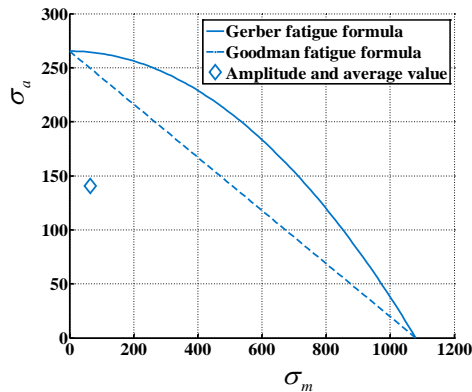
According to the Von-Mises criterion, equivalent stress σ_m and σ_a are calculated by the following formula (Li, 2016):

$$\sigma_e = \frac{1}{\sqrt{2}} \sqrt{(\sigma_x - \sigma_y)^2 + (\sigma_y - \sigma_z)^2 + (\sigma_z - \sigma_x)^2 + 6(\tau_{xy}^2 + \tau_{yz}^2 + \tau_{zx}^2)} \quad (13)$$

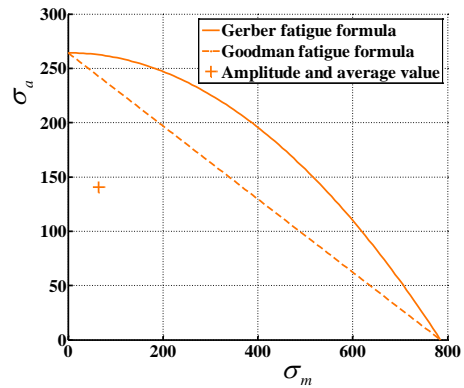
Tab. 6. Equivalent stress of four typical FS materials

Materials	Mean stress (σ_m)	Stress amplitude (σ_a)
12Cr2Ni4	64.57	140.71
20CrMnSi	64.69	140.60
30CrMoA	64.73	141.35
40CrNiMoA	64.39	140.76

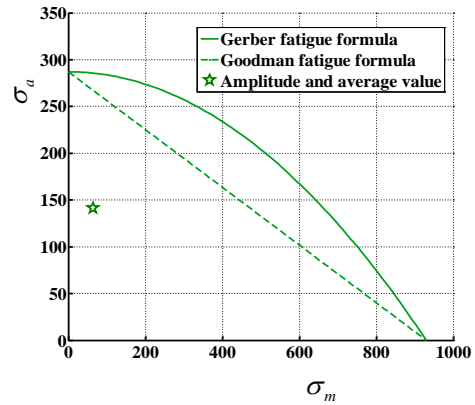
Given the equivalent stress σ_m and σ_a , the ultimate fatigue stress σ_1 , and stress limit σ_b , Gerber and Goodman fatigue limit formulas are plotted in Fig. 10.



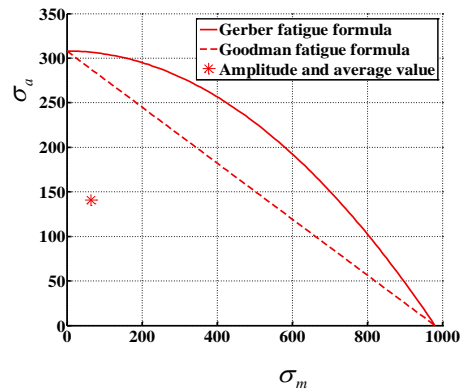
(a) Fatigue limit formula of 12Cr2Ni4



(b) Fatigue limit formula of 20CrMnSi



(c) Fatigue limit formula of 30CrMoA



(d) Fatigue limit formula of 40CrNiMoA

Fig.10. Fatigue limit formulas of four typical FS materials

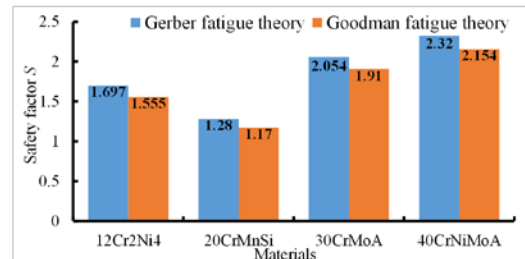


Fig. 11. Safety factor of four typical FS materials under 109 cycles

The transverse coordinate is the strength limit σ_b of the material, and the longitudinal coordinate is

the ultimate fatigue stress σ_{-1} under fixed cycle times. In Fig. 9, it is evident that the stress value of 10^9 cycles is the ultimate fatigue stress σ_{-1} . Based on this graph, safety factor of FS of material 12Cr2Ni4, 20CrMnSi, 30CrMoA and 40CrNiMoA can be accurately calculated. The safety coefficient of different materials is compared in Fig. 11.

CONCLUSIONS

In this article, we have determined the weakest area in the fatigue life of FS through the analysis of the working condition. The differential equation of thin-walled cylinder and a developmental FEM approach have been combined to study two different types of stress: bending stress, caused by the support of the wave generator, and meshing stress, related to the load torque. The maximum radial, circumferential and shear stress of bending and meshing stress are extracted and synthesized separately, and the stress spectrum of FS tooth root in three directions is formed. At last, the fatigue life of four typical FS materials is compared. Some conclusions are summarized as follows:

(1) The solutions to the bending stress were derived by building the differential equations of thin-walled cylinder. The normal stress σ_1 , σ_2 and shear stress τ_{12} of FS at different α , φ are calculated by importing boundary condition and deformation function. The distribution of bending stress has a strong periodicity. In terms of amplitude, the circumferential stress amplitude is the largest and the shear stress amplitude is the smallest.

(2) A developmental FEM method was adopted to extract the multi-tooth meshing stress after calculating the theoretical meshing tooth number of the involute tooth profile. The average stress in the zone of engaging-in is higher than that in the zone of engaging-out, which is due to the impact of engaging.

(3) The fatigue life evaluation is carried out based on Goodman and Gerber fatigue theories. The results indicated that the safety coefficient of fatigue life of material 40CrNiMoA is at least 12.95% higher than the other three materials. This provides a useful reference guide for us to evaluate fatigue life and choose appropriate material.

ACKNOWLEDGEMENTS

The research is supported by Beijing Science and Technology Major Project coded D17110400590000, Jing-Hua Talents Project of Beijing University of Technology and the National Natural Science Foundation coded 51805012.

REFERENCES

- C. W. Musser, "Breakthrough in mechanical drive design-the harmonic drive," *Machine Design*, Vol. 32, No. 8, pp. 160-173 (1996).
- C. W. Musser, "Strain Wave Gearing," *United States patent*, No.2906143 (1959)
- D. Vassileva, Y. Kiyosawa and M. Suzuki, "Sensorless Torque Control for a Robot with Harmonic Drive Reducers," *Mechanics Based Design of Structures & Machines*, Vol. 39, No.2, pp. 253-267 (2011).
- Liu W., "Finite calculation and ansys on the column-shaped flexspline of harmonic drive," *Chinese Journal of Mechanical Engineering*, Vol. 42, No. 4, pp. 52-57 (2006).
- Zou C., Tao T. and Jiang G., "Deformation and stress analysis of short flexspline in the harmonic drive system with load," *IEEE International Conference on Mechatronics and Automation*. IEEE, pp. 676-680 (2013).
- Zu L., Yin A and Sun Y, "Deformation Analysis and Simulation of the Cup-Shaped Flexspline for Harmonic Drive Using in Aerocrafts," *International Journal of Computer Theory and Engineering*, Vol. 8, No. 6, (2016).
- Tuttle T. D., "Understanding and Modeling the Behavior of a Harmonic Drive Gear Transmission," *Massachusetts Institute of Technology*, (1992).
- Jeong K. S., Dai G. L. and Oh S. H., "Development of the composite flexspline for a cycloid-type harmonic drive using net shape manufacturing method," *Composite Structures*, Vol. 32, No. s1-4, pp. 557-565 (1995).
- Gandhi P. S., "Modeling and control of nonlinear transmission attributes in harmonic drive systems," *Rice university*, (2001).
- Preissner C., Royston T. J. and Shu D., "A High-Fidelity Harmonic Drive Model," *Dissertations & Theses - Gradworks*, Vol. 134, No. 1, pp. 11002-11013 (2012).
- Donghui MA, Jianing WU and Yan S. Z., "A method for detection and quantification of meshing characteristics of harmonic drive gears using computer vision," *Science China: Technological Sciences*, Vol. 59, No. 9, pp. 1305-1319 (2016).
- Chao Z., Wang S. and Wang Z., "An accelerated life test model for harmonic drives under a segmental stress history and its parameter optimization," *Chinese Journal of Aeronautics*, Vol. 28, No. 6, pp. 1758-1765 (2015).
- Gravagno F., Mucino V. H. and Pennestrì E., "Influence of wave generator profile on the pure kinematic error and centrodes of harmonic drive," *Mechanism & Machine Theory*, Vol. 104, pp. 100-117 (2016).
- Zhang H., Ahmad S. and Liu G., "Modeling of Torsional Compliance and Hysteresis Behaviors in Harmonic Drives," *IEEE/ASME Transactions on Mechatronics*, Vol. 20, No. 1, pp. 178-185 (2014).
- Chen X., Liu Y. and Xing J., "The parametric design

- of double-circular-arc tooth profile and its influence on the functional backlash of harmonic drive,” *Mechanism & Machine Theory*, Vol. 73, No. 2, pp. 1-24 (2014).
- Tjahjowidodo T., Al-Bender F. and Brussel H. V., “Theoretical modelling and experimental identification of nonlinear torsional behaviour in harmonic drives,” *Mechatronics*, Vol. 23, No. 5, pp. 497-504 (2013).
- Han B., Ma J. and Li H., “Research on nonlinear friction compensation of harmonic drive in gimbal servo-system of DGCMG,” *International Journal of Control Automation & Systems*, Vol. 14, No. 3, pp. 779-786 (2016).
- Gao W., Furukawa M. and Kiyono S., “Cutting error measurement of flexspline gears of harmonic speed reducers using laser probes,” *Precision Engineering*, Vol. 28, No.3, pp. 358-363 (2004).
- Shi Z., Li Y., Liu G., “Adaptive torque estimation of robot joint with harmonic drive transmission,” *Mechanical Systems & Signal Processing*, Vol. 96, pp. 1-15 (2017).
- Routh B., Maiti R., Ray A. K., “Aspects of lubrication at the wave generator - flexspline interface in strain wave gearing units,” *International Gear Conference*, pp. 709-720 (2014).
- Ostapski W. and Mukha I., “Stress state analysis of harmonic drive elements by FEM,” *Bulletin of the Polish Academy of Sciences Technical Sciences*, Vol. 55, No. 1, pp. 115-123 (2007).
- Ostapski W., “Analysis of the stress state in the harmonic drive generator-flexspline system in relation to selected structural parameters and manufacturing deviations,” *Bulletin of the Polish Academy of Sciences Technical Sciences*, Vol. 58, No. 4, pp. 683-698 (2011).
- Kikuchi M., Nitta R. and Kiyosawa Y., “Stress Analysis of Cup Type Strain Wave Gearing,” *Key Engineering Materials*, 243-244:129-134 (2003).
- Han S. J. and Oh S. H., “A study on stress and vibration analysis of a steel and hybrid flexspline for harmonic drive,” *Composite Structures*, Vol. 47, No. 1-4, pp. 827-833 (1999).
- Kayabasi O., Erzincanli F., “Shape optimization of tooth profile of a flexspline for a harmonic drive by finite element modelling,” *Materials & Design*, Vol. 28, No. 2, pp. 442-447 (2007).
- Folega P., “Analysis of stress state of toothed ring of flexspline by means the BEM,” *Archives of Materials Science & Engineering*, Vol. 59, No. 1, pp. 40-45 (2013).
- Xiang Q. and Yin Z., “Investigation of temperature effect on stress of flexspline,” *Applied Mathematics and Mechanics*, Vol. 35, No. 6, pp. 791-798 (2014).
- Sahoo V. and Maiti R., “State of Stress in Strain Wave Gear Flexspline Cup on Insertion of Drive Cam Experiment and Analysis,” *World Congress on Engineering*, (2015).
- Xu Z., “Elastic mechanics (Fifth Edition: volume II),” *Higher Education Press*, pp. 173-177 (2016).
- Ren Y. B. and Xu L. Z., “Analysis on the Finite Element of Electromechanic Coupling of Flexible Gear in Electromagnetic Harmonic Drive,” *Applied Mechanics and Materials*, 249-250:771-777 (2012).
- Fu G., “An Extension of Hertz's Theory in Contact Mechanics,” *Journal of Applied Mechanics*, Vol. 74, No. 2, pp. 373-374 (2007).
- Starke P., Walther F. and Eifler D., “Fatigue assessment and fatigue life calculation of quenched and tempered SAE 4140 steel based on stress - strain hysteresis, temperature and electrical resistance measurements,” *Fatigue & Fracture of Engineering Materials & Structures*, Vol. 30, No. 11, pp. 1044-1051 (2010).
- Li Shuting, “Diaphragm stress analysis and fatigue strength evaluation of the flex-spline, a very thin-walled spur gear used in the strain wave gearing,” *Mechanism and Machine Theory*, Vol. 104, pp. 1-16 (2016).

彎扭作用下諧波減速器杯型柔輪應力分析與壽命評價

蔡力鋼 胡秋實 劉誌峰 楊聰彬 張濤
北京工業大學先進制造技術北京市重點實驗室

摘要

本文旨在研究杯型柔輪多齒嚙合的復合應力計算和壽命評價方法。為了準確描述柔輪齒根的應力狀態，將數學方法和仿真方法相結合，根據應力的類型，將柔輪分為兩部分：杯體部分和齒輪部分。對於杯體部分，利用微分方程和邊界條件計算彎曲應力。對於齒輪部分，建立齒部模型，在扭轉作用下進行了仿真分析，得到齒輪嚙合應力。最終根據彎曲和扭轉應力，復合得到徑向應力、周向應力和剪切應力的應力譜。在應用第四強度理論計算馮·米塞斯應力後，根據應力-壽命曲線和疲勞極限公式，進行了不同材料疲勞壽命安全系數的對比分析。